Appl. Phys. B (2013) 112:529–537
DOI 10.1007/s00340-013-5435-0

Applied Physics B
Lasers and Optics

Algebraic tomographic reconstruction of two-dimensional gas temperature based on tunable diode laser absorption spectroscopy

Junling Song · Yanji Hong · Guangyu Wang · Hu Pan

Received: 24 October 2012 / Accepted: 23 March 2013 / Published online: 8 April 2013

Abstract Based on tunable diode laser absorption spectroscopy, the combustion gas temperature distribution was reconstructed using the algebraic iterative reconstruction technique. The effects of the projected angle and number of rays on the temperature reconstruction results for both fan beam and parallel beam were investigated. The flow field information was shown in detail. The reconstruction quality increased with increased ray number for both parallel- and fan-beam projections. The trend tended to be smooth when the total number of beams exceeded 100. A virtual ray method combined with the reconstruction algorithms was proposed. The virtual ray method is effective to improve the accuracy of reconstruction results for the symmetric and non-axisymmetric temperature distributions. Moreover, the temperature reconstruction of an infrared gas-field furnace is demonstrated, showing the virtual ray method can be applied to the combustion diagnostics.

1 Introduction

Tunable diode laser (TDL) absorption spectroscopy is characterized by fast response, sensitivity, non-invasiveness. Thus, this technique is used to measure the flow field temperature, gas composition, mass flux, and other quantities in a wide range of practical applications. For in situ measurements, TDL sensors have been deployed in the turbofan (PW6000) inlet [1], scramjet engine inlet [2], and scramjet isolator/combustor for the maintenance of engine performance [3–8].

TDL sensors traditionally provide a path-averaged temperature along the laser beam because of its line-of-sight property that limits the technique of producing uniform flow fields. However, significant temperature and concentration gradients exist for most combustion cases. One method of overcoming this problem is to extend the absorption information along the laser beam where multiple absorption transitions are used [9, 10]. Another method is to combine the absorption spectroscopy technique with image reconstruction technique to obtain the internal structure of the region of interest. The two-dimensional (2D) spatially resolved distribution of the temperature and concentration reconstruction can be produced by a reconstruction algorithm.

Two general categories are divided into two groups: one are the transform-based methods including Abel inversion [11] and Filtered Back Projection algorithm (FBPA) [12, 13], the other are iterative technique, such as Algebraic Reconstruction Technique (ART) [14, 15] and Maximum Likelihoon–Expectation Maximization (ML-EM) [16]. Abel inversion is often used with the assumption of spherically symmetry or axially symmetry [17, 18]. For the FBPA, the drawbacks include the need for large beam lines and intensive projection angles to ensure undistorted reconstruction [19, 20]. To decrease the number of projected angles, the ART is widely employed because of its better reconstruction performance in cases of incomplete projection angles and few beam projections. Kasyutich et al. [21] reconstructed a non-axisymmetric temperature and concentration distribution using the ART. In the experiment, four servomotors were adopted to control the detector and emitter, and the measurement would spend about 160 s. In some cases, a fast data collection is needed

J. Song (✉) · Y. Hong · G. Wang · H. Pan
State Key Laboratory of Laser Propulsion and Applications, Academy of Equipment, P.O Box 3380-86, Huairou District, Beijing 101416, China
e-mail: songjl@mail.ustc.edu.cn

because the experiment would be completed in a few milliseconds. Therefore, the emitters and detectors are fixed in a certain location to save the acquisition time [22, 23]. Wang et al. [24] set up four laser platforms where each laser rotated forming 11° fan, collecting data in 100 ms. Ma et al. [25, 26] introduced hyperspectral absorption spectroscopy to tomographic reconstruction by a simulated annealing algorithm in which the number of projections can be reduced. However, a large wide-scan laser or more than four lasers are needed to satisfy the requirement of more than 10 transitions.

A parallel beam [3, 25], fan beam [19, 21] or an irregular and sparse beam arrangement [23, 27, 28] can be chosen by laser absorption tomography. Terzija et al. [27] proposed an optimization strategy that used only 27 optical paths through the subject for the engine cylinder. Twynstra et al. [28] explained the optimization method using mathematical matrices. Above two researches both use irregular beam arrangements, aiming at reducing the number of beams that brings about complex optical system. In the present study, the parallel- and fan-beam arrangements are adopted to find an optimal optical layout.

In optimal algorithm studies, Piccolomini et al. [29] developed a regularized solution that was efficient for the computation of least-squares normal equations. To shorten the iterations, Li et al. [29] introduced a modified adaptive algebraic tomographic reconstruction technique with an auto-adjustment relaxation parameter. Hansen et al. [31] put forward several strategies to choose the optimal relaxation parameter and termination rules.

In a practical combustor, the installation of numerous optical sensors in a limited space is impossible. Therefore, an optimal sensor distribution plays an important role in tomographic reconstruction. This paper begins with a short review of the absorption spectroscopy theory and ART in Sect. 2. Then, the numerical model and optical layout are described in Sect. 3. Sect. 4 presents the simulation results, including the influences of the projected angles and number of rays per angle on the temperature reconstruction. Moreover, a virtual ray method is proposed and verified with few projected rays though simulation. The experimental validation of the virtual ray method is shown in Sect. 5. Concluding remarks are given in Sect. 6.

2 Theory

Two major components, absorption spectroscopy and tomography, are needed to solve two-dimensional water vapor distribution. To facilitate the discussion, this section provides a brief summary of the theories of temperature measurement based on the direct absorption spectroscopy and tomography.

2.1 Fundamental spectroscopy for temperature measurement

An isolated transition centered at frequency v through a uniform medium of length L (cm) is described by the Beer-Lambert law

$$\ln\left(\frac{I_t}{I_0}\right) = -k_v L = -P\chi S_i(T)\Phi(v)L \tag{1}$$

where I_0 and I_t are the incident and transmitted laser intensities, respectively. k_v (cm^{-1}) is the spectral absorption coefficient, P (atm) is the total pressure of the gas, χ is the mole fraction of the absorbing species of interest, $S_i(T)$ (cm^{-2} atm^{-1}) is the line strength of the transition at temperature T (K), $\phi(v)$ is the Voigt line shape function.

The line strength $S_i(T)$ can be calculated by the following scaling relationship

$$S(T) = S(T_0)\frac{Q(T_0)}{Q(T)}\frac{T_0}{T}\exp\left[-\frac{hcE''}{k}\left(\frac{1}{T}-\frac{1}{T_0}\right)\right] \times\left[1-\exp\left(-\frac{hcv_0}{kT}\right)\right]\left[1-\exp\left(-\frac{hcv_0}{kT_0}\right)\right]^{-1} \tag{2}$$

where $S(T_0)$ is the line strength at reference temperature, E'' (cm^{-1}) is the low-state energy of the transition, h (J s), c (cm s^{-1}), and k (J K^{-1}) are the Planck's constant, light speed, and Boltzmann's constant, respectively. Q(T) is the partition function, which can be written by an polynomial expression of temperature [32].

Combined Eqs. 1 and 2, the ratio of the absorbance measured by two transitions reduces simply to the ratio of line strengths

$$R = \frac{S_1(T)}{S_2(T)} = \frac{S_1(T_0)}{S_2(T_0)}\exp\left[-\left(\frac{hc}{k}\right)\left(E_1''-E_2''\right)\left(\frac{1}{T}-\frac{1}{T_0}\right)\right] \tag{3}$$

The relative sensitivity can be written as

$$\left|\frac{\mathrm{dR/R}}{\mathrm{dT/T}}\right| = \left(\frac{hc}{k}\right)\frac{\left|\left(E_1''-E_2''\right)\right|}{T} \tag{4}$$

Then the gas temperature is determined by Eqs. 2 and 3, which can be expressed as

$$T = \frac{\frac{hc}{k}\left(E_2''-E_1''\right)}{\ln\frac{A_1}{A_2}+\ln\frac{S_2(T_0)}{S_1(T_0)}+\frac{hc}{k}\frac{\left(E_2''-E_1''\right)}{T_0}} \tag{5}$$

$$\frac{A_1}{A_2} = \frac{\int P_{abs}L\Phi_{v_1}\chi S_1(T)\mathrm{dv}}{\int P_{abs}L\Phi_{v_2}\chi S_2(T)\mathrm{dv}} = \frac{S_1(T)}{S_2(T)} \tag{6}$$

where A is the integrated absorbance. The selection criteria for the optimal pair of transitions have been discussed in detail elsewhere [4, 6, 33]. Based on the criteria, the line pair of 7,205.25 and 7,416.05 cm^{-1} is selected for the

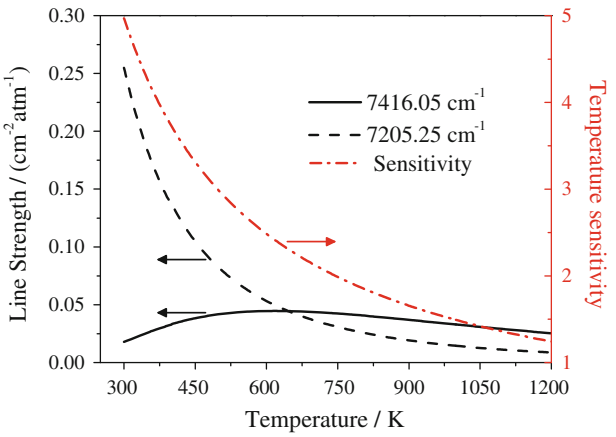

Fig. 1 Line strength and temperature sensitivity of H_2O absorption transitions at 7,416.05 and 7,205.25 cm^{-1}

simulation temperature within 300–1,300 K. The spectroscopy parameters of the transitions used in this study are based on HITRAN 2008 database [34]. Figure 1 shows the line strength and the relative sensitivity versus temperature.

2.2 Tomographic image reconstruction

Tomographic image reconstruction is the process of spatially reconstructing the region of interest from the transmission or reflection data by illuminating the object from many directions. The process can be separated into two steps. The first step is projection at multiple angles. Parallel- and fan-beam geometries are mostly used for the collection. The number of rays and rotation angle for each projection are the two major parameters that directly influence data collection by the detector. The second step is processing, which involves the transformation of data using a certain reconstruction algorithm. In many applications, such as in an isolator and combustor, space within which to assemble so many emitters and detectors is also limited. The iteration method, which uses a small number of rays and a few projections, seems to be the optimal method. In this study, ART is adopted to obtain the 2D temperature distribution.

The region of interest f (x, y) is discretized to $N = n \times n$ square grid points, where the gas parameters such as temperature, pressure and species concentration are assumed to be constant, as illustrated in Fig. 2.

When a ray i passes through the region, the integrated absorbance can be written as a discretization expression.

$$A_{v,i} = \sum_{j=1}^{N} f_{v,j} L_{ij} = \sum_{j=1}^{N} [PS(T)X]_{v,j} L_{ij} \tag{7}$$

where the subscript i and j represent the beam ($i = 1, 2, \ldots M$) and grid points ($j = 1, 2, \ldots N$, $N = n^2$), v is transition frequency, respectively. L_{ij} is the length that ray i crosses to

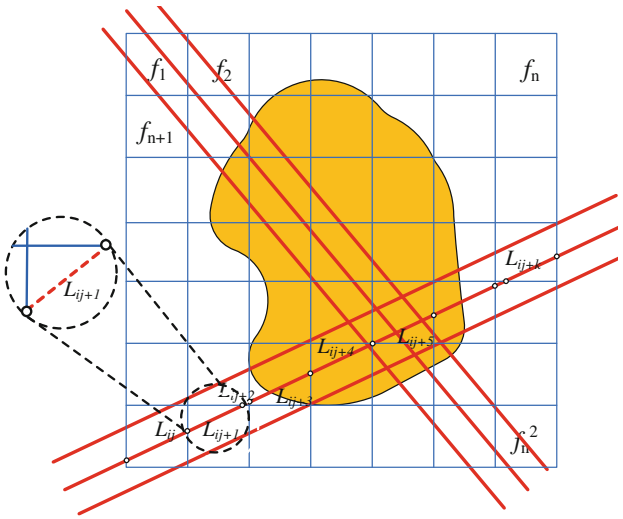

Fig. 2 Algebraic method that divides the image area into *square grids* where the value of the reconstruction is assumed to be constant

span grid point j. L_{ij} is not changed once the number of rays and projection angle are fixed. When the total number of rays is M for projection, Eq. (7) can be expressed as

$$\begin{bmatrix} L_{11} & L_{12} & \cdots & \cdots & L_{1N} \\ L_{21} & L_{22} & \cdots & \cdots & L_{2N} \\ \vdots & \vdots & \vdots & \vdots & \vdots \\ L_{M1} & L_{M2} & \cdots & \cdots & L_{MN} \end{bmatrix} \times \begin{bmatrix} f_1 \\ f_2 \\ \vdots \\ \vdots \\ f_N \end{bmatrix} = \begin{bmatrix} A_1 \\ A_2 \\ \vdots \\ A_M \end{bmatrix} \tag{8}$$

where subscript v in Eq. (7) has been omitted in Eq. (8) and the following Eqs. (9, 10, 11, 12). The matrix L is a sparse matrix because only one beam at most can cross grid points of $2n$–1. The application of ART solves Eq. (8) in the iterative equation as follows [12]

$$\vec{f}^{(k)} = \vec{f}^{(k-1)} - \alpha \frac{\left(\vec{L}_i \cdot \vec{f}^{(k-1)} - A_i\right)}{\vec{L}_i \cdot \vec{L}_i} \vec{L}_i \tag{9}$$

where the superscript k represents the iteration index in ART, the subscript i represents the beam ($i = 1, 2, \ldots M$), α is the relaxation parameter. To accelerate convergence, the iteration equations are added to an automatically changing relaxation parameter given by Ref. [30]

$$\begin{aligned} \vec{f}^{(k)} &= \vec{f}^{(k-1)} - \vec{\alpha}^{(k)} \left(\vec{L}_i \cdot \vec{f}^{(k-1)} - A_i\right) \\ \alpha_j^{(k)} &= \beta \times (f_j^{k-1} L_{i,j}) / \sum_{j=1}^{N} f_j^{k-1} L_{i,j} \end{aligned} \tag{10}$$

where the subscript i represents the beam ($i = 1, 2, \ldots M$) and grid point ($j = 1, 2, \ldots N$), β is a constant with value of 0.6. In this problem, the temperature and concentration

reconstructions should be non-negative. Therefore, a constraint is added to the reconstruction algorithms. As expressed in Eq. (11), Φ denotes the projection onto the positive image. Then, the projections are incorporated into each step of the iterations [31]

$$[\Phi(f)]_j = \begin{cases} f_j, f_j \geq 0 \\ 0, \text{ else} \end{cases}$$
$$\overrightarrow{f}^{(k)} \leftarrow \Phi\left(\overrightarrow{f}^{(k-1)} - \alpha_k\left(\overrightarrow{L}_i \cdot \overrightarrow{f}^{(k-1)} - A_i\right)\right) \tag{11}$$

Moreover, a smoothness regulation is applied to reduce the discrepancy among the nearest grid points, which is expressed as

$$f_{(m,n)}^{k} = (1-\delta) \times f_{(m,n)}^{(k-1)} + \delta \times \left(\sum_{y=n-1}^{n+1}\sum_{x=m-1}^{m+1} f_{(x,y)}^{(k-1)}/8\right) \tag{12}$$

where δ is 0.006. The kth iterated result of $f_{(m,n)}^{k}$ relates not only to the k-1th result of $f_{(m,n)}^{(k-1)}$, but also to the nearby grid points. The details are shown in Refs. [25, 35].

3 Numerical models

3.1 Original temperature distribution

Using a Gaussian function, a model of temperature distribution between 300 and 1,300 K is created, as shown in Fig. 3. Two beam geometries, fan- and parallel-beam, are used to determine the effect of the ray number and projection angles in the tomography system.

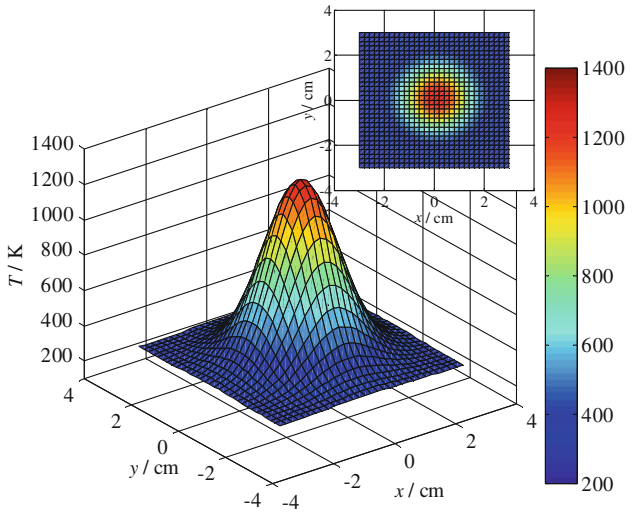

Fig. 3 Original temperature model. The viewpoint is specified in terms of azimuth −37.5° and elevation 30°, and the inset is a plan view

3.2 Beam arrangement

The optical beam arrangements are shown in Fig. 4. For the fan-beam projection, the fan-beam sources are placed along a circle with the equal space. The radius of the circle equals to the length of the reconstruction region. The angle of each fan-beam source is 90°, which contains p rays arranged with an equal angle. Each time the fan-beam source rotates with angle θ, the projection data of p rays are calculated. For ART method, the region of interest can be still reconstructed in the incomplete projection condition. In our present study, a comparison of fan-beam with parallel-beam arrangement would be carried out. Therefore, an equal rotation angle is used, and the total number of the rays is $M = 360p/\theta$.

In the parallel model, the rotation angle is 45° distributing in 180°. As shown in Fig. 4b, Δd_{grid} represents the length of the grid and Δd_{line} is the interval between the two rays. In addition, d_{line} from the first ray to the last ray is $\sqrt{2}$ times to the edge of the square test d_{grid}. In this condition, d_{line} just equals to the length of the reconstruction region,

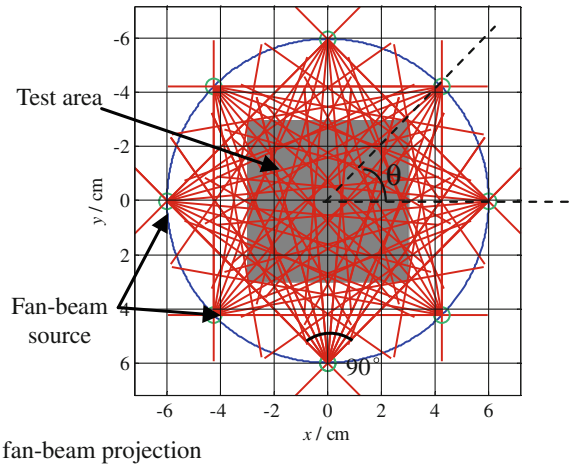

(a) fan-beam projection

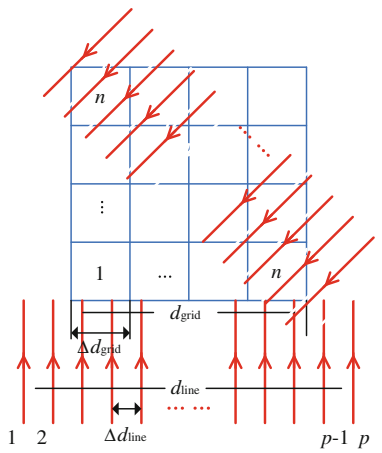

(b) parallel-beam projection

Fig. 4 Optical beam arrangements

and at least one ray crosses the grid point when the projection angle equals 45° or 135°.

4 Simulation results and discussion

4.1 Effect of number of rays

Using the parallel projection, the area of interest is separated into 11 × 11, 21 × 21, and 31 × 31 grid points and four projected angles (0, 45°, 90° and 135°) are used. For each condition, four different numbers of rays are utilized to determine the effect of the rays on the 2D temperature reconstruction. Part of the reconstruction results are shown in Fig. 5. Poor reconstruction usually appears on the corner and the centre of the reconstruction area. Each projection equation represents a path value of a ray, as expressed in Eq. (8). Taking $p_0 = 16$, 31 × 31 grids; for example, there are 64 (4 projected angles × 16 rays per projected angle) projection equations, containing temperature unknowns of 961. In the iteration, an initial guess assigns the grids, and then the grid value is changed when a ray crosses through the grid. As shown in Fig. 5a–d, more projective rays indicate a nearer reconstruction image to the origin. When the area of interest is divided into a small number of grid points, such as Fig. 5e, f, a rough description is shown.

To quantify the quality of the reconstructed temperature, the normalized mean absolute distance measures *DevT* is defined as

$$DevT = \sqrt{\frac{1}{n \times n}\sum_{l=1}^{n}\sum_{s=1}^{n}\left[\frac{\left(T_{l,s}^{cal} - T_{l,s}^{orig}\right)}{T_{\max}^{orig} - T_{\min}^{orig}}\right]^2} \tag{13}$$

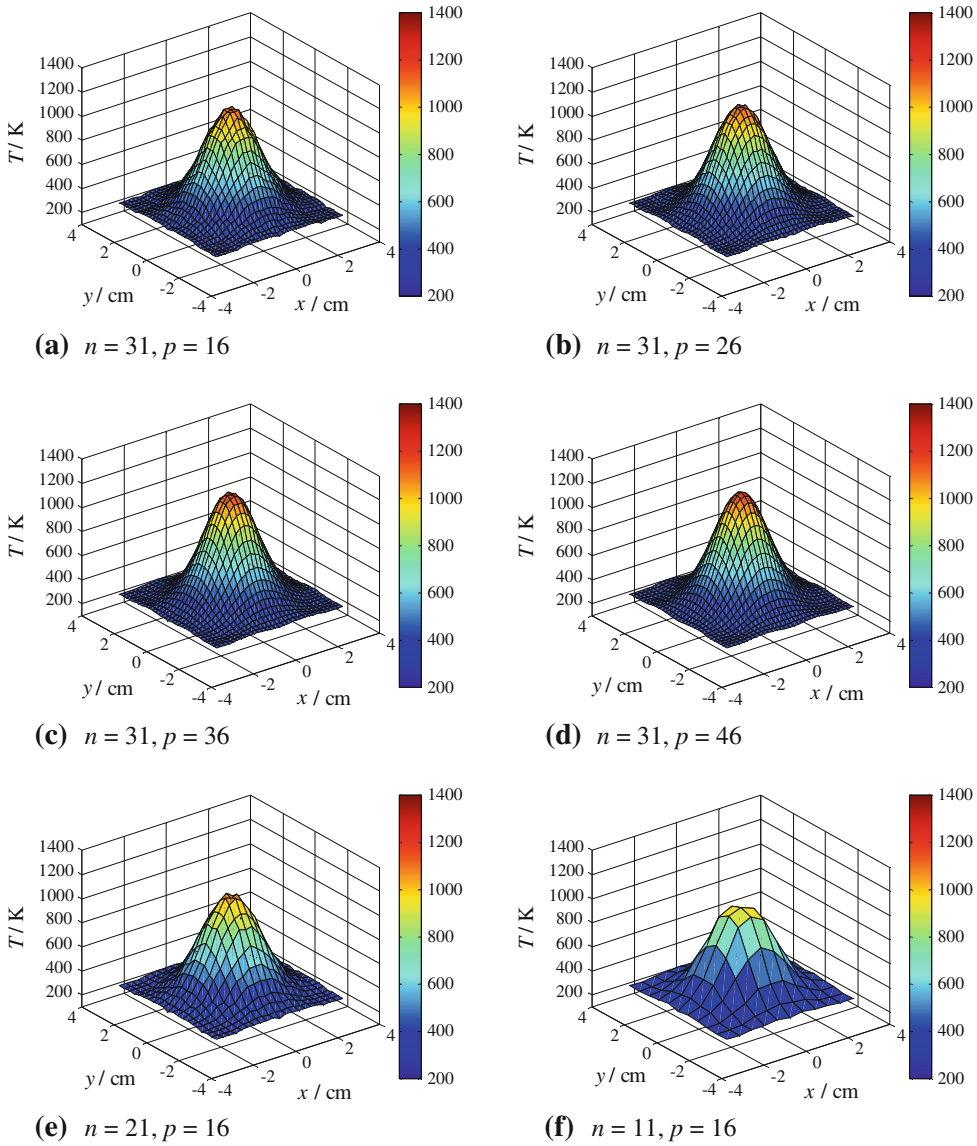

Fig. 5 Reconstructed temperature for different grid points and ray numbers. Parallel projection and four detection angles are applied

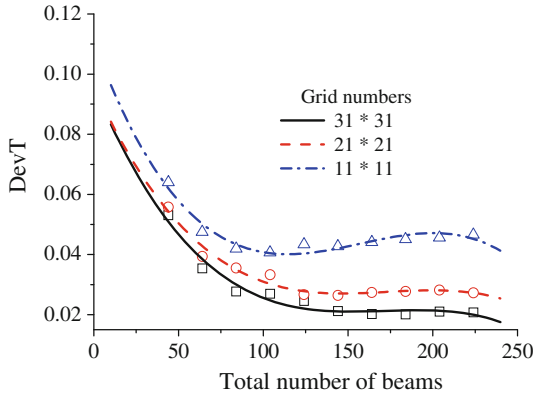

(a) Parallel-beam projection

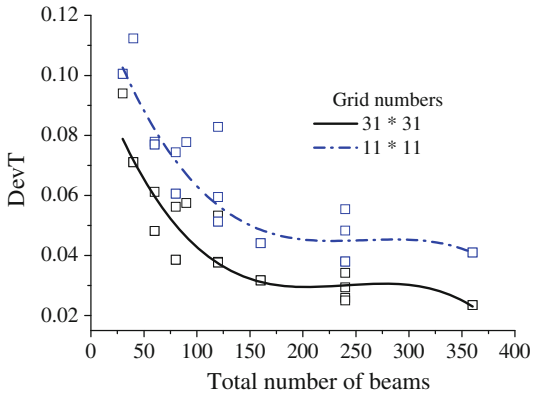

(b) Fan-beam projection

Fig. 6 Normalized mean absolute error versus beam number ($n = 31$, 21 and 11) for parallel- and fan-beam projection

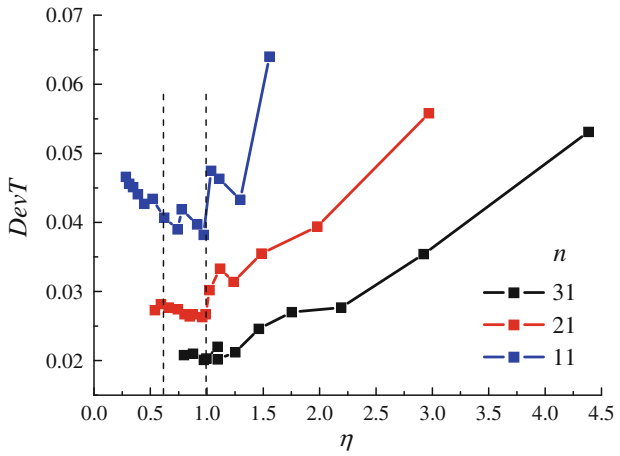

Fig. 7 *DevT* versus η for different grid points

where up-script *cal* and *orig* denote the calculated and original values, respectively. The down-script l and s represent the grid point number.

For the fan-beam projection, different rotation angles (30°, 45°, 60°, 90°, and 120°) and three different numbers of rays (10, 20, and 30) for each projection are selected in the simulation.

The calculated results are shown in Fig. 6. *DevT* decreases with the increased beam number for both parallel- and fan-beam projections. Moreover, the trend tends smooth when the beam number exceeds 100. The dense 31 × 31 grids perform better reconstruction than the other two distributions for the same beam number. The parallel-beam projection obtains a lower *DevT* than the fan-beam projection because the parallel projection has to rotate only half circle when the beam number is the same as that of the fan-beam projection. The fan-beam forms a non-uniform pattern, which causes a course grid in the region of interest. Therefore, in cases where the object under investigation is more or less homogeneously distributed over the detection area (and not in the vicinity of the fan centers), parallel-beam projection leads to better reconstruction results. Besides, the parallel projection also allows for a simple and compact assembly system.

The relationship between the number of grid points and number of projection for each angle is important to optimize the ray establishment. For the parallel-beam projection, we quantify the relationship by η as follows

$$\eta = \Delta d_{line} / \Delta d_{grid} \tag{14}$$

Figure 7 plots the relationship between *DevT* and η at different grids. When η is between 0.6 and 1, *DevT* is located at a low level, wherein the temperature reconstruction achieves good results. As η exceeds 1, *DevT* significantly increases because the small numbers of rays result in few even number of rays crossing through some grids. Therefore, the optimal ray–grid distribution of η is between 0.6 and 1.

4.2 Virtual ray method

In reality, temperature fields are in a continuum of states. Therefore, a higher number of the discrete grid points enable, more details are to be known. In Sect. 4.1, an improvement is observed when the number of rays and number of grid points increase. However, the rays for each projection are usually no more than 20 because of limited experimental space and cost.

In this study, we propose a virtual ray method. Some virtual rays are added to the reconstruction algorithms. As shown in Fig. 8, two new rays i'_{3n+1} and i'_{3n+2} are inserted in i_n and i_{n+1}, so the interval between two rays Δd_{line} changes to $\Delta d_{\text{line}}/3$ and the total number of rays changes to $3p - 2$. According to the optimal ray–grid distribution, we choose η equals 1 in this simulation, to make the number of grid points which will be nine times the initial.

The absorbance for the new rays can be calculated from the initial absorbance, which can be written as follows

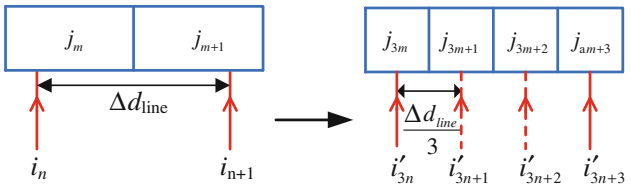

Fig. 8 Scheme of the virtual ray method. The *dash line* i'_{3n+1} and i'_{3n+2} represent two virtual rays inserted i_n in i_{n+1}, and the marks i_n and i_{n+1} change to i'_{3n} and i'_{3n+3} to avoid confusing in the virtual ray method

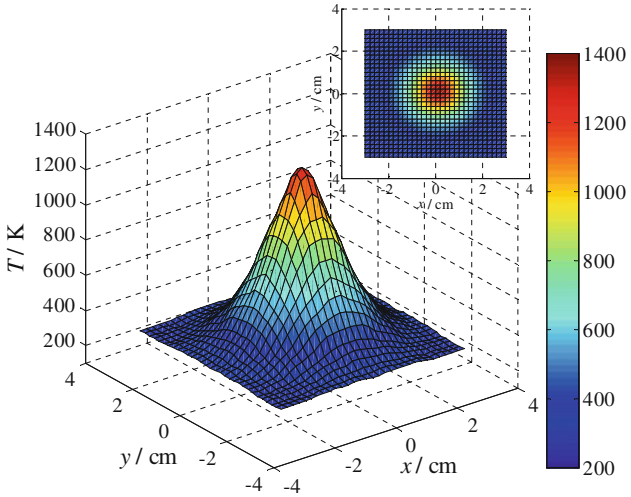

Fig. 9 Reconstructed temperature using the virtual beam method. 16 rays of each projection and four detection angles are adopted

$$\begin{aligned} A_{i'3n} &= A_{i_n} \\ A_{i'3n+1} &= \frac{2}{3}A_{i_n} + \frac{1}{3}A_{i_{n+1}} \\ A_{i'3n+2} &= \frac{1}{3}A_{i_n} + \frac{2}{3}A_{i_{n+1}} \\ A_{i'3n+3} &= A_{i_{n+1}} \end{aligned} \tag{15}$$

where A_{i_n} and $A_{i_{n+1}}$ are the absorbance of ray i_n and i_{n+1}, respectively. The reconstructed temperature by the virtual ray method is shown in Fig. 9. 31 × 31 grid, 16 rays for each projection are used in the simulation. Comparing with Fig. 5a, e, f, the noise is significantly reduced. Meanwhile, detailed flow field information can be obtained.

Three different numbers of rays (11, 16, and 21) and three different grids (11 × 11, 21 × 21, and 31 × 31) are selected to test the virtual ray method. Moreover, 100 random Gaussian phantoms with off-centering are used in the test. To ensure the high temperature region in the area of interest, the maximal temperature in the borer of the area is no more than 476 K. One of the random phantoms and the reconstruction are shown in Fig. 10, in which 31 × 31 grids and 16 rays are chosen.

The results of the simulations are summarized in Table 1, where '31-revise-centre' represents the results

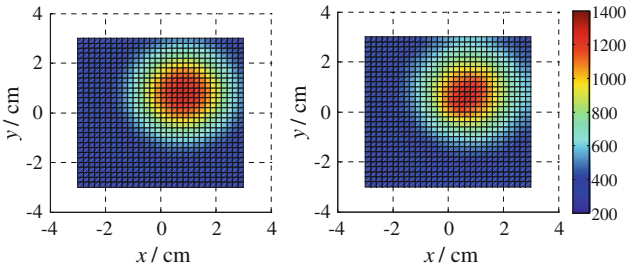

Fig. 10 Off-centered Gaussian phantom (*left*) and the reconstructed temperature profile (*right*)

Table 1 Normalized mean absolute error (*DevT*) for different grid numbers

n	p_0		
	11	16	21
31	0.0531	0.0354	0.0277
21	0.0558	0.0394	0.0355
11	0.064	0.0475	0.0419
31-revise-centre	0.0522	0.0271	0.0207
31-revise-random	0.0444	0.0283	0.0221

based on model in Fig. 3, '31-revise-random' means the results of 100 random Gaussian phantoms. The last two conditions are tested using the virtual ray method with 31 × 31 grid. We found that a lower *DevT* is apparently obtained by the virtual ray method compared with other simulations. For the non-axisymmetric temperature distribution, the virtual ray method is still efficient for the reconstructions.

5 Experiment on the combustion test

An optical layout used for temperature and concentration measurements in the horizontal plane is shown in Fig. 11. The total area of the test is 33 × 33 cm. A circular infrared gas-field furnace with a diameter of 14 cm is mounted onto a stepped motor to be scanned by the laser. The height of the laser beam plane is 1 cm above the plane of the furnace. Two DFB lasers at 1,344.9 and 1,388.1 nm (NEL) are separately mounted into two thermo-electric cooler controller mounts (ILX, LDC-3908; ThorLabs, ITC502), respectively. The two lasers are coupled by a single mode fiber to a 50/50 Oz Optics 1 × 2 fiber splitter. One beam passes through the area of interest, and is collected by a multimode fiber. The other passes through the etalon (ThorLabs, SA200-12A) with a free spectral range of 0.05 cm^{-1}. Time division multiplexing technology is adopted to obtain each laser signal. The direct scanning

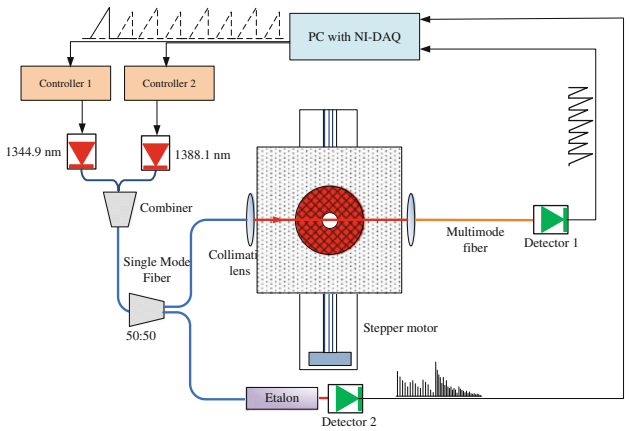

Fig. 11 Schematic of the parallel projection laser absorption system for 2D temperature and concentration reconstruction

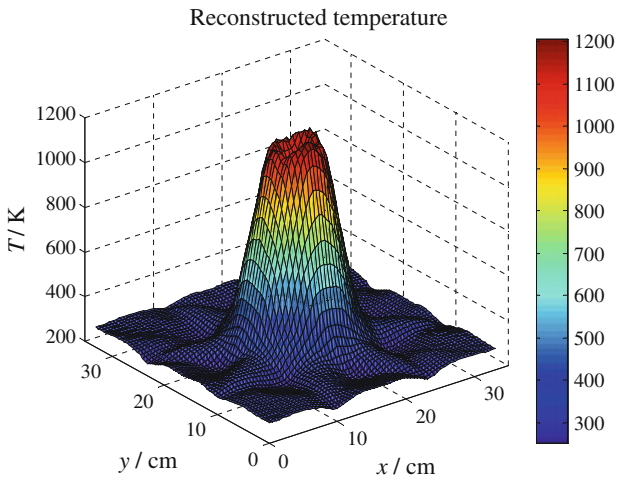

Fig. 12 Temperature reconstruction using 97 as the number of projection rays

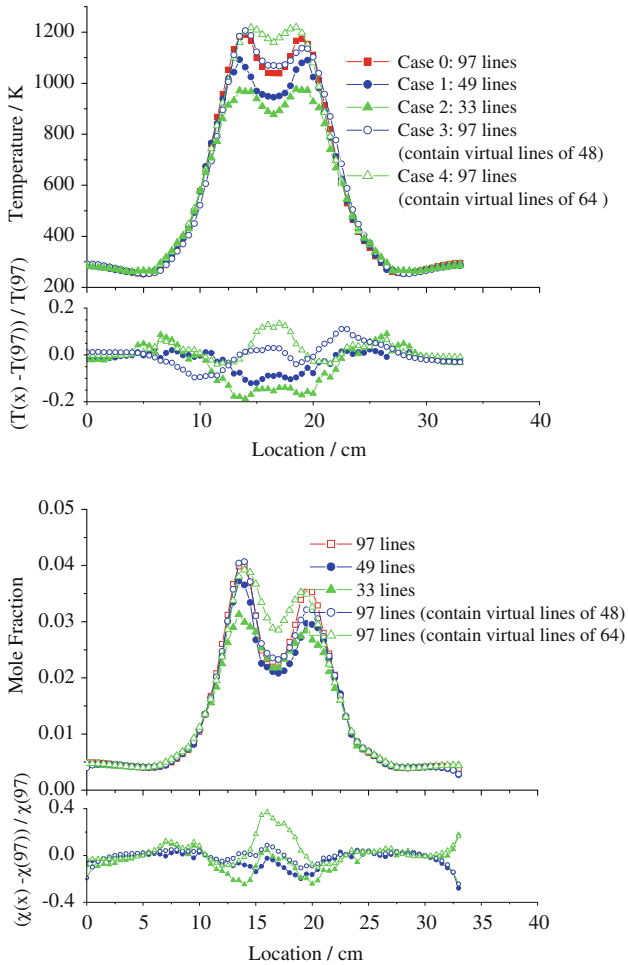

Fig. 13 Temperature and concentration reconstruction for different cases (along the x axis, $y = 0$)

functions of time division are generated by DAQ computer using a 12-bit National Instruments PCI-6115 A/D board. Under the control of the program, the furnace is moved with a distance of 0.5 cm at the speed of 2 cm/s. 100-period signals (100 ms) are recorded at each furnace position to collect statistics of the projection signals. After recording the detector signal, the furnace is transferred to a new position. When the furnace has been scanned along the horizontal direction, the plane of the furnace is rotated 90° and the above procedure is repeated. A LabView code is developed for data acquisition and analysis. The raw projection data are stored in the computer for further processing and 2D temperature reconstruction. The experimental spectra are fitted by Voigt line shape functions. In principle, a more accurate analysis of the integrated absorption areas for the non-uniform temperature distribution can achieve by a hybrid Voigt fit scheme [9] or the standard Humlíček algorithm [36].

The reconstructed value through four projection angles (0, 45°, 90°, and 135°) is shown Fig. 12. Each angle has 97 rays, and the distance between the first and the last ray is 48 cm. The projection value is ignored when the ray does not pass through the area of interest. A low temperature area appears in the middle of the furnace because of the existence of a 3 cm diameter hole. To demonstrate the virtual ray method, we calculate four cases: cases 1 and 2 have the intervals between the two rays (1 and 1.5 cm); case 3 has one virtual ray added between two rays based on case 1; and case 4 has two virtue rays added between two rays based on case 2. For each case, the distance between the first and last rays at 48 cm, and the numbers of projection rays are 49, 33, 97 (containing 48 virtual rays), and 97 (containing 64 virtual rays), respectively.

The reconstructed temperature and concentration results are shown in Fig. 13. For case 1 and 2, the reconstructed temperature and concentration are lower than case 0 condition in high temperature area. The reconstruction quality significantly improves for case 3 when 48 virtual rays are added to the reconstruction procedure. However,

nearly 15 % remains in the middle-low temperature area for case 4, because the gradient of the temperature in this area is large. Despite the fact that the number of rays for reconstructed calculation is 97, the number of real rays is very small to reveal the real distribution. This finding indicates that the virtual ray method can improve the reconstruction quality, but applications with large gradient are unsuitable.

6 Conclusion

Using Gaussian function, a model of temperature distribution between 300 and 1,300 K is reconstructed using ART. Parallel- and fan-beam projections are chosen to test the influence of the numbers of rays and grid points. The normalized mean absolute distance *DevT* that represents the reconstruction quality, decreases with increased beam number for both beam projections. Moreover, the trend is smooth when the total number of beams exceeds 100. The reconstruction value also depends not only on the number of rays, but also on the number of grid points. An optimal ray–grid establishment shows the distance from between two nearby rays to the length of the grid ranges from 0.6 to 1. A virtual ray method is proposed and experimentally demonstrated to improve the reconstruction quality efficiently. The reconstruction noise is found to be significantly decreased, and the detailed flow field information can be obtained.

Acknowledgments This work is supported by the National Natural Science Foundation of China (Grant Nos.11102234). The authors would like to thank all the referees and editors for their valuable suggestions to improve the contents of the paper, and extend special thanks to Dr. Fang Juan and Dr. Wang Diankai for their assistant with temperature reconstruction experiments.

References

1. K.H. Lyle, J.B. Jeffries, R.K. Hanson, AIAA J. **45**, 2204 (2007)
2. M.F. Miller, W.J. Kessler, M.G. Allen, Appl. Opt. **35**, 4905 (1996)
3. M. S. Brown, AIAA. 0555 (2012)
4. X. Zhou, X. Liu, J.B. Jeffries, R.K. Hanson, Meas. Sci. Technol. **16**, 2437 (2005)
5. O. Witzel, A. Klein, S. Wagner, C. Meffert, C. Schulz, V. Ebert, Appl. Phys. B **109**, 521 (2012)
6. M.G. Allen, Meas. Sci. Technol. **9**, 545 (1998)
7. X. Liu, J.B. Jeffries, R.K. Hanson, K.M. Hinckley, M.A. Woomansee, Appl. Phys. B. **82**, 469 (2006)
8. C.D. Lindstrom, K.R. Jackson, S. Williams, R. Givens, W.F. Bailey, C.J. Tam, W.F. Terry, AIAA J. **47**, 2368 (2009)
9. S.T. Sanders, J. Wang, J.B. Jeffries, R.K. Hanson, Appl. Opt. **40**, 4404 (2001)
10. X. Liu, J.B. Jefferies, R.K. Hanson, AIAA J. **45**, 411 (2007)
11. L.M. Smith, D.R. Keefer, S.I. Sudharsanan, J. Quant. Spectrosc. Radiat. Transfer **39**, 367 (1988)
12. L.A. Shepp, B.F. Logan, IEEE T. Nucl. Sci. **21**, 21 (1974)
13. G.T. Herman, *Fundamentals of computerized tomography: image reconstruction from projections* (Springer, New York, 2009)
14. R. Gordon, R. Bender, G.T. Herman, J. Theor. Biol. **29**, 471 (1970)
15. A.C. Kak, M. Slaney, *Principles of computerized tomographic imaging* (IEEE Press, New York, 1999)
16. J. Llacer, J.D. Meng, IEEE Trans. Nucl. Sci. **32**, 855 (1985)
17. C.J. Dasch, Appl. Opt. **31**, 8 (1992)
18. R. Villarreal, P.L. Varghese, Appl. Opt. **44**, 6786 (2005)
19. K. M. Busa, E. Bryner, J. C. McDaniel, C. P. Goyne, C. T. Smith, G. S. Diskin, AIAA. **1294**, 1–14 (2011)
20. J. Song, Y. Hong, G. Wang, High Power Laser Part. Beam **24**, 2073 (2012)
21. V.L. Kasyutich, P.A. Martin, Appl. Phys. B **102**, 149 (2011)
22. S.J. Carey, H. McCann, F.P. Hindle, K.B. Ozanyan, D.E. Winterbone, E. Clough, Chem. Eng. J. **77**, 111 (2000)
23. P. Wright, C.A. Garcia-Stewart, S.J. Carey, F.P. Hindle, S.H. Pegrum, S.M. Colbourne, P.J. Turner, W.J. Hurr, T.J. Litt, S.C. Murray, S.D. Crossley, K.B. Ozanyan, H. McCann, Appl. Opt. **44**, 6578 (2005)
24. F. Wang, K.F. Cen, N. Li, J.B. Jeffries, Q.H. Huang, J.H. Yan, Y. Chi, Meas. Sci. Technol. **21**, 045301 (2010)
25. L. Ma, W. Cai, Appl. Opt. **47**, 3751 (2008)
26. L. Ma, W. Cai, A.W. CasWell, T. Kraetscher, S.T. Sanders, S. Roy, J.R. Gord, Opt. Express **17**, 8602 (2009)
27. N. Terzija, J.L. Davidson, C.A. Garcia-Stewart, P. Wright, K.B. Ozanyan, S. Pegrum, T.J. Litt, H. McCann, Meas. Sci. Technol. **19**, 094007 (2008)
28. M.G. Twynstra, K.J. Daun, Appl. Opt. **51**, 7059 (2012)
29. E.L. Piccolomini, F. Zama, Appl. Math. Comput. **102**, 87 (1999)
30. N. Li, C. Weng, Chin. Opt. Lett. **9**, 061201 (2011)
31. P.C. Hansen, M.S. Hansen, J. Comput. Appl. Math. **236**, 2167 (2012)
32. R.R. Gamache, S. Kennedy, R. Hawkins, L.S. Rothman, J. Mol. Struct. **517–518**, 407 (2000)
33. X. Zhou, X. Liu, J.B. Jeffries, R.K. Hanson, Meas. Sci. Technol. **14**, 1459 (2003)
34. L.S. Rothman, I.E. Gordon, A. Barbe, D. Chris Benner, P.F. Bernath, M. Birk, V. Boudon, L.R. Brown, A. Campargue, J.P. Champion, K. Chance, L.H. Coudert, V. Dana, V.M. Devi, S. Fally, J.M. Flaud, R.R. Gamache, A. Goldman, D. Jacquemart, I. Kleiner, N. Lacome, W.J. Lafferty, J.Y. Mandin, S.T. Massie, S.N. Mikhailenko, C.E. Miller, N. Moazzen-Ahmadi, O.V. Naumenko, A.V. Nikitin, J. Orphal, V.I. Perevalov, A. Perrin, A. Predoi-Cross, C.P. Rinsland, M. Rotger, M. Šimečková, M.A.H. Smith, K. Sung, S.A. Tashkun, J. Tennyson, R.A. Toth, A.C. Vandaele, J. Vander Auwera, J. Quant. Spectrosc. Radiat. Transfer. **110**, 533 (2009)
35. J. Song, Y. Hong, G. Wang, H. Pan, Acta Phys. Sin. **61**, 240702 (2012)
36. J. Humlíček, J. Quant. Spectrosc. Radiat. Transfer **27**, 437 (1982)